Oxygen Vacancy Filament-Based Resistive Switching in $Hf_{0.5}Zr_{0.5}O_2$ Thin Films for Non-Volatile Memory

Mark Kracklauer[1, 2], Fabian Ambriz-Vargas[1], Gitanjali Kolhatkar[1], Bernhard Huber[1, 2], Christina Schindler[2], Andreas Ruediger[1]*

[1]Institut Nationale de la Recherche Scientifique, Centre Énergie, Matériaux, Télécommunications, 1650 Boulevard Lionel-Boulet, Varennes, Québec, J3X 1S2, Canada.
[2]Munich University of Applied Sciences, Department of Applied Sciences and Mechatronics, Lothstrasse 34, 80335 Munich, Germany

*Corresponding author: Tel: (001) 514 228 6854; E-mail: ruediger@emt.inrs.ca

Received: 14 August 2018, Revised: 18 September 2018 and Accepted: 30 October 2018

DOI: 10.5185/amlett.2019.2225
www.vbripress.com/aml

Abstract

The continued evolution of electronic devices relies on the development of new semiconductor memory technology. Given the high compatibility of the $Hf_{0.5}Zr_{0.5}O_2$ thin films with the CMOS technology, we investigate the charge transport mechanisms that occur in a relative thick $Hf_{0.5}Zr_{0.5}O_2$ thin film (4 to 6 nm-thick) when subjected to electrical stresses. To that end we fabricate $Hf_{0.5}Zr_{0.5}O_2$ heterostructures with a Pt tip as the top electrode and TiN and Pt as bottom electrode by radio-frequency magnetron sputtering. After analyzing the surface morphology of the as-received and as-deposited films by atomic force microscopy, the transfer of the desired chemical stoichiometry from the sputtering target to the substrate surface is studied by Raman spectroscopy. The ferroelectricity of the $Hf_{0.5}Zr_{0.5}O_2$ thin films is confirmed by piezoresponse force microscopy measurements, and a retention of 22 h is obtained, attesting to the non-volatility of the samples. Nano-scale electrical measurements reveal the presence of resistive switching, where the low resistance state (ON state) in both Pt-tip/$Hf_{0.5}Zr_{0.5}O_2$/TiN and Pt-tip/$Hf_{0.5}Zr_{0.5}O_2$/Pt heterostructures can be created by the formation of a conductive filament based on oxygen vacancies. Copyright © VBRI Press.

Keywords: Electrical charge transport mechanism, thin films, CMOS compatible, nanoscale characterization.

Introduction

Recent technology improvements in micro- and nano-fabrication techniques have brought a new generation of electronic devices to the market, such as computers, cellphones, cameras or tablets. In addition to being slimmer, faster and lighter, these devices possess more storage capacity, while providing an improved camera resolution. As predicted by "Moore's law", customers have been experiencing the birth of new generations of electronic devices every couple of years, during the last four decades [**1**]. This trend has led the customers to continually expect more powerful and cheaper devices. However, that may not be the case if the electronic industry continues working with the current semiconductor memory technology.

The key issue with current electronic devices is that they rely on the performance of a set of different semiconductor memories that have already reached their physical limits [**2**]. In general, the processor within the central processing unit (CPU) of any personal computer is serviced by a series of memory technologies (Memory hierarchy) [**3**]. The closest memory to the CPU is called "*Cache memory*", which is comprised of a static random access memory (SRAM). This memory is very fast (write/erase time: 0.3 ns/ 0.3 ns) but it is relatively large in cell size (six transistors with a minimum cell size of $140F^2$, where "*F*" is the minimum feature size). Given their physical properties, SRAMs are used to provide fast access to instructions and data to the processor. In the next level of the hierarchy appears the "*Principal memory*", which is comprised of a dynamic random access memory (DRAM). Contrary to SRAM, it is more compact (one-transistor and one-capacitor, with a cell size of $6F^2$) but it is slower (write/erase time: 10ns/10ns). The physical properties of DRAM allow it to reach high densities on a memory chip. The "*Principal memory*" is used to store and to process temporary information from the solid state hard drive, which is also referred to as "*Secondary memory*" [**3**]. In both cases, the "*Cache*" and the "*Principal*" memories are volatile, as the stored information will not remain when the energy power supply is turned off. The "*Secondary memory*" consists mainly of a flash memory, an external memory with a

non-volatile nature as it holds the information when the power supply is turned off. In comparison to the "*Primary and Cache memories*" it is really slow (write/erase time: 1ms/10ms) [**3**].

Therefore, the dominant memory types in modern electronics are dynamic-RAM (DRAM), static-RAM (SRAM), and flash memories (FLASH). For many decades these memory technologies have been successfully scaled down to achieve higher speeds and increased density of memory chips at lower cost [**4**]. However, they have gradually approached their physical limits of scalability. Therefore, for further advance in information processing/storage technologies, it is necessary to develop a universal memory that can replace the aforementioned conventional memories [**2, 3**]. This universal memory should combine the non-volatile nature of FLASH with the high scalability of DRAM, high speed of SRAM and high endurance of DRAM and SRAM.

Among the different noticeable types of emerging memories, a promising candidate for the universal memory is the resistive random access memory (Re-RAM) [**5**]. A Re-RAM consists of an insulating material sandwiched between two metallic electrodes. The application of a high electrical stress (DC voltage) leads to the formation of a conductive filament inside the insulating material which induces changes in the electrical resistance state of the memory cell. These two states consist of a high- and a low- resistance state, and can be regarded as "1" and "0" in a binary code [**1, 2**]. Re-RAM provide the advantage of requiring low power consumption while offering high-speed as well as good scalability. In order to bring this memory type onto the market, it is necessary to ensure the slow use of complementary metal oxide semiconductor (CMOS) compatible materials. Hafnium zirconium oxide ($Hf_{0.5}Zr_{0.5}O_2$) has been identified as a promising material for such applications. While Hafnia (HfO_2) and Zirconia (ZrO_2), are already widely used in the semiconductor industry [**6-9**] as dielectric layers in current commercial devices such as DRAMs and ferroelectric field effect transistors (Fe-FETs), $Hf_{0.5}Zr_{0.5}O_2$ presents a high CMOS compatibility due to its low crystallization temperature. In previous work, we fabricated resistive switching-based memory devices using ultra-thin (2.8 nm) ferroelectric $Hf_{0.5}Zr_{0.5}O_2$ films and direct tunneling [**7**]. Here, we report on the development ReRAM that exploit thicker $Hf_{0.5}Zr_{0.5}O_2$ films, (4-6 nm) and oxygen vacancies as the main charge transport mechanism. Such devices are CMOS compatible and can be used in the development of a universal memory.

Experimental

Thin film deposition

$Hf_{0.5}Zr_{0.5}O_2$ thin films were deposited on TiN/Si substrates and conductive polycrystalline Si/SiO_2/ Pt substrates by on-axis radio frequency (RF) magnetron sputtering. The sputtering unit consisted of a computer-controlled table top deposition system from Plasmionique Inc. (SPT310 model). A polycrystalline $Hf_{0.5}Zr_{0.5}O_2$ ceramic disc (2.54 cm in diameter and 0.317 cm thickness) was used as a sputtering target. Prior to deposition, the chamber was evacuated at a base pressure of ~ 10^{-5} Torr using a dry pumping station. An Ar and O_2 mixture (oxygen partial pressure, $Po=O_2/(Ar+O_2)$ = 50%) composed the sputtering medium with an operating pressure in the range of 5 – 30 mTorr. The RF power was fixed to 20 Watts on the target and the substrate temperature was maintained at 500°C during deposition. The target surface was cleaned for 15 minutes by pre-sputtering prior to all depositions while keeping the shutter on the substrate surface closed. In order to eliminate contaminations and to maintain the target composition's homogeneity, the target-substrate distance was kept constant at 110 mm. A summary of the deposition parameters for $Hf_{0.5}Zr_{0.5}O_2$ and TiN thin films (resistance equal to 1kΩ) is provided in **Table 1**.

Table 1. Summary of sputtering conditions used for the deposition of $Hf_{0.5}Zr_{0.5}O_2$ and TiN thin films.

Film:	**TiN**	**$Hf_{0.5}Zr_{0.5}O_2$**
Target:	TiN	$Hf_{0.5}Zr_{0.5}O_2$
Substrate:	(100) Si	TiN/(100) Si
Power density:	~4 W/cm^2	~4 W/cm^2
Medium:	Ar and N_2	Ar and O_2
Pressure:	10 mTorr	5 mTorr
Temperature:	500°C	500°C
Deposition time:	240 min	20-200 min

Microstructural and chemical characterization

The surface morphology of the as-grown $Hf_{0.5}Zr_{0.5}O_2$ samples was investigated by atomic force microscopy (AFM, Smart SPM 1000-AIST-NT, Inc.) in intermittent mode, using silicon cantilevers tips with typical tip radii of ~10 nm. The layer thickness of the ceramic film was determined by X-ray reflectivity (XRR, Philips X'pert Materials Research Diffractometer). Raman scattering measurements were performed with a Horiba system and a 473 nm solid state blue Cobolt 05-02 laser. In this system, a Horiba Scientific Synapse Back-Illuminated Deep Depletion 1024 ×256 CCD was employed as detector and the laser was focused on the sample through a 0.9 NA 100× objective.

Electrical and ferroelectric characterization

Ferroelectric switching of the films was studied by piezo response force microscopy (PFM) using conductive Pt-Ir-coated silicon cantilever tips (radius of ~30nm). Nanoscale electrical measurements were performed in conductive AFM (C-AFM) mode, with the Pt-Ir-coated silicon cantilever tips acting as a top electrode. Local current–voltage *(I-V)* characteristics were measured by positioning a conductive Pt-Ir- coated silicon tip at a selected point on the surface of $Hf_{0.5}Zr_{0.5}O_2$ thin film and performing a "DC" voltage sweep.

Results and discussion

$Hf_{0.5}Zr_{0.5}O_2$ thin films were deposited on a TiN/Si substrate. The surface morphology of the TiN conductive layer is presented in **Fig. 1 (a)**. This AFM scan shows that the TiN thin film has an atomic flat surface (rms of ~0.5 nm), an attractive characteristic for semiconductor memory applications [**10**] as the use of conductive electrodes with uniform flat surfaces results in a large ON/OFF ratio [**10**]. **Fig. 1(b)** presents the surface morphology of $Hf_{0.5}Zr_{0.5}O_2$ thin films deposited on the surface of the TiN conductive layer. From this figure it can be seen that the microstructure of the $Hf_{0.5}Zr_{0.5}O_2$ is constituted of small grains that uniformly cover the complete surface of the TiN conductive electrode. From the surface morphology of $Hf_{0.5}Zr_{0.5}O_2$, the grain size was estimated to ~10 nm. However, in literature a typical grain size of 3-7 nm is commonly report in ultrathin $Hf_{0.5}Zr_{0.5}O_2$ films [**11, 12**]. The observed discrepancy can be attributed to the limit of the AFM system in which the resolution is determined by the tip radius of the silicon probe (~10 nm). Therefore, the grain size of the as-deposited $Hf_{0.5}Zr_{0.5}O_2$ thin films investigated here is lower than the observed 10 nm.

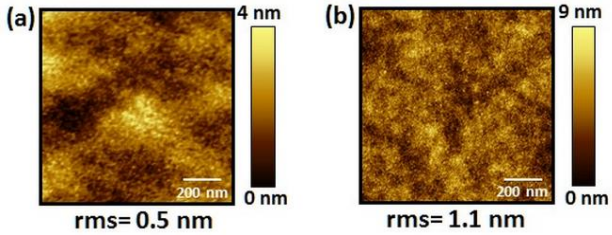

Fig. 1. Surface morphology of the as deposited (a) TiN and (b) $Hf_{0.5}Zr_{0.5}O_2$ thin films.

Prior to chemical analysis, the deposition rate of $Hf_{0.5}Zr_{0.5}O_2$ inside the sputtering chamber was determined. To that end, four $Hf_{0.5}Zr_{0.5}O_2$ samples were deposited under similar sputtering conditions (Table 1) but for different deposition times (60, 80, 135, and 200 minutes). The XRR spectrum of each sample is shown in **Fig. 2(a)**. We can see that all four samples present multiple oscillations, indicating a smooth surface (rms roughness ~1.4 nm) [**7**]. Using the software "X'pert reflectivity", the layer thickness of each sample was determined as depicted in **Fig. 2(b)**. This figure reveals a linear relationship between layer thickness and deposition time, with a relatively low deposition rate (~5 nm per hour).

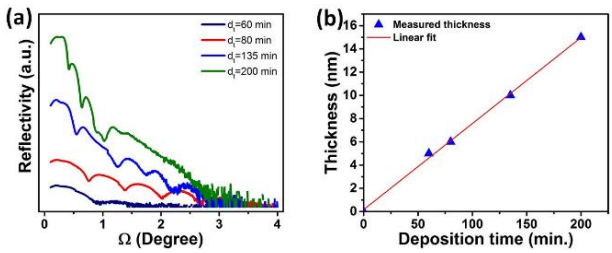

Fig. 2. (a) XRR spectra, where d_t corresponds to the deposition time and (b) calculated layer thickness of different $Hf_{0.5}Zr_{0.5}O_2$ films.

The deposition process of the $Hf_{0.5}Zr_{0.5}O_2$ film by RF-magnetron sputtering occurs in three steps. First, the appropriate atomic species (Hf, Zr and O) are produced at the target surface, second, the atomic species are transported to the substrate, and last, the atomic species nucleate and grow of on the substrate [**13, 14**]. The inappropriate selection of the synthesis parameters can affect the transfer of the target stoichiometry. Therefore, we investigated the transfer of the target stoichiometry to the substrate by Raman spectroscopy. Raman measurements were performed on the $Hf_{0.5}Zr_{0.5}O_2$ sputtering target as well as on the as-deposited $Hf_{0.5}Zr_{0.5}O_2$ films. For this analysis, it was necessary to make the film deposition on Pt substrates, as the Raman signal of the TiN/Si substrates overshadows that of the $Hf_{0.5}Zr_{0.5}O_2$ thin film. $Hf_{0.5}Zr_{0.5}O_2$ can adopt different crystal structures such as monoclinic, tetragonal, or orthorhombic, and each phase is characterized by different Raman modes [**15, 16**]. In $Hf_{0.5}Zr_{0.5}O_2$, only 6 of the 18 normal modes are allowed Raman modes in the tetragonal phase [**17, 18**]. On the other hand, while 18 out of the 36 normal modes are allowed Raman modes in $Hf_{0.5}Zr_{0.5}O_2$ in monoclinic phase, only a small fraction of these modes is usually observed at room temperature. In bulk form, $Hf_{0.5}Zr_{0.5}O_2$ is stable in the monoclinic phase at room temperature [**17, 18**]. Consistently, Raman modes, characteristic of the monoclinic phase, are observed on the $Hf_{0.5}Zr_{0.5}O_2$ target (**Fig. 3(a)**). The Raman spectrum of the as-deposited $Hf_{0.5}Zr_{0.5}O_2$ (**Fig. 3(b)**) presents the main characteristics of the monoclinic and tetragonal phases. $Hf_{0.5}Zr_{0.5}O_2$ thin films can present two types of phases (monoclinic and tetragonal) which can coexist. Indeed, the morphology of $Hf_{0.5}Zr_{0.5}O_2$ in thin film form is composed of small grains that are subjected to either compressive or tensile strain, thereby resulting in the formation of two different phases [**14**]. These results confirm that the sputtering parameters described in the experimental section allow the right transportation of the chemical species from the target to the substrate surface.

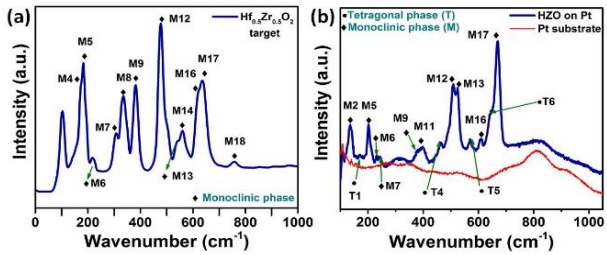

Fig. 3. Typical Raman spectra obtained from a (a) sputtering target and (b) as-deposited $Hf_{0.5}Zr_{0.5}O_2$ thin film. The Raman spectrum of the Pt substrate is also included for comparison.

One of the main characteristics of $Hf_{0.5}Zr_{0.5}O_2$ is its ferroelectric character in ultrathin film form. Therefore, we investigated the ferroelectric behavior of a 4 nm-thick $Hf_{0.5}Zr_{0.5}O_2$ film deposited on a TiN/Si substrate. This characterization was carried out by drawing two square patterns of different polarization on the $Hf_{0.5}Zr_{0.5}O_2$ film surface, using a biased Pt/Ir probe (**Fig. 4**). First, an

upward ferroelectric polarization of the $Hf_{0.5}Zr_{0.5}O_2$ surface was created by applying a negative bias ($V_{tip} - 9V$) over a large surface region (3 µm × 3 µm) of the as-deposited film (blue square, dark region). Subsequently, a smaller square region (1.5 µm × 1.5 µm) with a downward ferroelectric polarization (green square, bright region) was formed by polarizing the surface of the as-deposited film with a positive bias ($V_{tip} + 9V$). This PFM analysis demonstrates that the 4 nm-thick $Hf_{0.5}Zr_{0.5}O_2$ film can have two different polarization states (upward and downward).

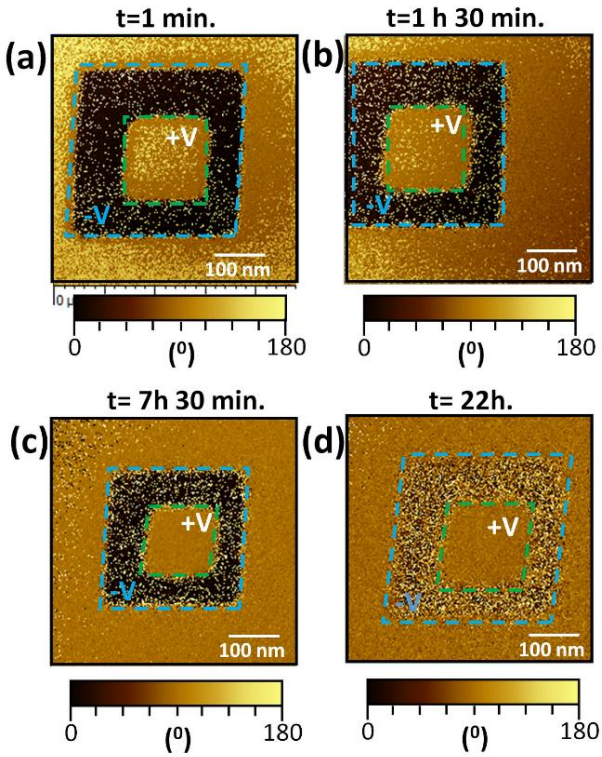

Fig. 4. Ferroelectric retention obtained for the surface of the as-deposited $Hf_{0.5}Zr_{0.5}O_2$ thin film (a) 1 min, (b) 1h30 min, (c) 7h30 min and (d) 22 h after poling.

Both states a can be used as binary data in a ferroelectric random access memory (Fe-RAM)[**19**] or used to modulate the electrical resistance in ferroelectric tunnel junction memory (FTJ) [**20, 21**]. Moreover, **Fig. 4** shows that the two polarization states can remain stable up to 22 hours, suggesting a non-volatile character [**9**].

After ensuring the ferroelectricity of the $Hf_{0.5}Zr_{0.5}O_2$ films, we investigated their electrical properties. We started by performing the electrical characterization of the TiN/4 nm-thick $Hf_{0.5}Zr_{0.5}O_2$/Pt tip system. A schematic representation of this memory cell is illustrated in **Fig. 5(a)**. Sweep voltages applied to this capacitor-like memory cell resulted in a hysteretic *I-V* behavior (**Fig. 5(b)**) characterized by two distinctive resistance states (high resistance state, HRS, and the low resistance state, LRS). In the LRS, the current increases linearly with the voltage. Based on literature, the origin of such an *I-V* hysteresis behavior is due to the formation of a conducting filament inside the $Hf_{0.5}Zr_{0.5}O_2$ insulating barrier [**3**]. This filament acts as a conductive bridge between the two electrodes. The formation of the conductive filaments can be attributed to different types of mechanisms, such as "Electrochemical metallization mechanism" where an electrochemically active metal is used as one of the electrodes in the memory cell [**3**]. In combination with an electric field, this leads to the formation of conductive metallic filaments made of the material composing the electrochemically active electrode. A reversal of the electric field results in the dissolution of the conductive filament and an increase in the electrical resistance (OFF state) [**3**]. Another switching mechanism is the "Valence change mechanism" where the conductive filament is made of oxygen vacancies [**5**]. The creation of such conductive filaments inside the insulating barrier is triggered by the migration of oxygen ions, which results in the formation of localized oxygen vacancies. The LRS in this kind of charge transport mechanism is attributed to electron hopping in the oxygen vacancies that are present inside of the insulating layer, while the HRS is caused by the rupture of the oxygen vacancies bridge [**5**].

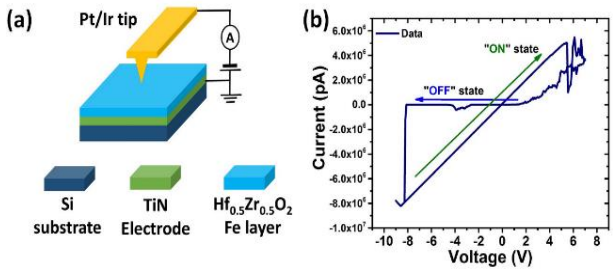

Fig. 5. (a) Schematic representation of the Pt-tip/$Hf_{0.5}Zr_{0.5}O_2$/TiN heterostructure and (b) local *I-V* curve obtained at 140°C from a 4 nm thin film.

Given that our Re-RAM memory cells are composed of inert electrodes (Pt and TiN), it is possible to discard electrochemical metallization mechanisms. If the $Hf_{0.5}Zr_{0.5}O_2$ oxide barrier is regarded as an insulating medium which can contain highly conducting domains (oxygen vacancies), the electrical current detected by the C-AFM in **Fig. 5(b)** can be attributed to valence change mechanism. The transition from the HRS to the LRS occurs during the application of a negative voltage which leads to the formation of conductive filaments inside of the $Hf_{0.5}Zr_{0.5}O_2$ thin film (**Fig. 6**). To verify this statement, the C-AFM was used to scan the surface of a 6 nm-thick $Hf_{0.5}Zr_{0.5}O_2$ thin film grown on a conductive inert electrode (Pt). An *I-V* curve obtained for this sample is presented in **Fig. 6(a)**. A topography image (**Fig. 6(b)**) taken after recording the *I-V* curve presents a hillock at the position where the voltage was applied during the C-AFM measurements (yellow dot in the center of the figure), while the current map acquired simultaneously displays an increase in electrical current (**Fig. 6(c)**, yellow dot). This figure demonstrates the formation of a conductive region at the position where the *I-V* curve was obtained, attesting to presence of bridge-based oxygen vacancies.

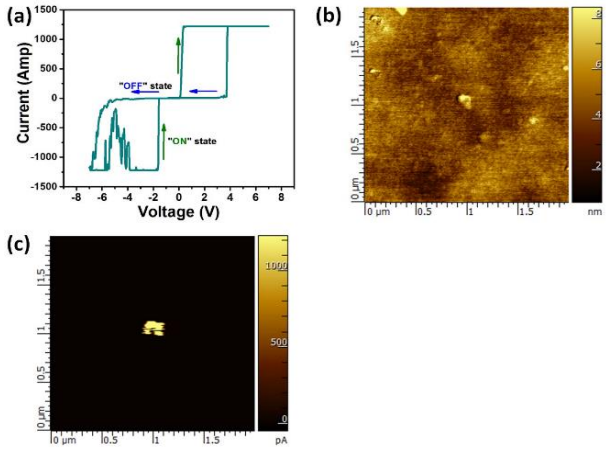

Fig. 6. (a) *I-V* curve obtained from a 6 nm-thick HZO film. (b) Topography image and (c) current map acquired after measuring the electrical behavior presenting an oxygen vacancy filament.

Conclusion

In summary, we investigate $Hf_{0.5}Zr_{0.5}O_2$ thin films for the universal memory. By combining AFM and Raman measurements, we reveal that the surface morphology of the $Hf_{0.5}Zr_{0.5}O_2$ thin films is composed of small grains in the monoclinic phase and in the tetragonal phase. Furthermore, PFM analysis confirms the presence of two ferroelectric polarization states (downward and upward) in our films, and that both ferroelectric states are stable for up to 22 hours, suggesting a non-volatile behavior. Finally, nanoscale measurements show that the application of high electrical stress on $Hf_{0.5}Zr_{0.5}O_2$ thin films with a thickness above 4 nm results in two different electrical resistance states (LRS and HRS) where the LRS state originates from an oxygen valance mechanism. These results attest to the potential of $Hf_{0.5}Zr_{0.5}O_2$ thin films with thicknesses above 4 nm for Re-RAM applications.

Acknowledgements

G. K. is thankful for an FRQNT Postdoctoral scholarship and F. A. V. for individual FRQNT MELS PBEEE 1M scholarship and for the financial support of CONACyT (National Council of Science and Technology-Mexico). M. K. and B. H. gratefully acknowledge financial support through the Bayerische Forschungsallianz. A. R. acknowledges generous support through an NSERC discovery and an NSERC strategic grant.

References

1. Baldi, L.; Bez, R.; Sandhu, G., *Solid-State Electron.* **2014,** *102*, 2.
2. Makarov, A.; Sverdlov, V.; Selberherr, S., *Microelectronics Reliability* **2012,** *52*, 628.
3. Jeong, D. S.; Thomas, R.; Katiyar, R. S.; Scott, J. F.; Kohlstedt, H.; Petraru, A.; Hwang, C. S., *Rep Prog Phys*, **2012**, *75*, 076502.
4. Joodaki, M., Springer Heidelberg New York Dordrecht London **2013**, 5.
5. Sawa, A., *Mater. Today*, **2008**, *11*, 28.
6. Ambriz-Vargas F.; R. T., A. Ruediger; Springer Nature Singapore Pte Ltd. **2018**.
7. Fabian, A. V.; Maxime Broyer, G. K.; Azza, Hadj-Youssef; Rafik Nouar; Andranik, Sarkissian; Thomas, Reji; Gomez-Yáñez, Carlos; Gauthier, Marc A.; Ruediger; A., *ACS Appl. Mater. Interfaces* **2017**, *9*, 13262.
8. Ambriz-Vargas, F.; Thomas, G. K., R.; Nouar, R.; Sarkissian, A.; Gomez-Yáñez, C.; Gauthier, M. A.; Ruediger A., *Appl. Phys. Lett.*, **2017**, *110*, 093106
9. Ambriz-Vargas, F.; Nouar, R.; Kolhatkar, G.; Sarkissian, A.; Thomas, R.; Gomez-Yáñez, C.; Gauthier, M. A.; Ruediger; A., *Mater. Today: Proceedings*, **2017**, *4*, 7000.
10. Garcia, V.; Bibes, M., *Nat Commun*, **2014**, *5*, 4289.
11. Materlik, R.; Künneth, C.; Kersch, A., *J. Appl. Phys.*, **2015**, *117*, 134109.
12. Kim, H. J.; Park, M. H.; Kim, Y. J.; Lee, Y. H.; Jeon, W.; Gwon, T.; Moon, T.; Kim, K. D.; Hwang, C. S., *Appl. Phys. Lett.*, **2014**, *105*, 192903.
13. Ambriz-Vargas, F.; Velasco-Davalos, I.; Thomas, R.; Ruediger, A., J. Vac. Sci. Technol., B: Nanotechnol.: Microelectron: Mater., Process., Meas., Phenom. **2016,** *34*, 02M101.
14. Hyuk Park, M.; Joon Kim, H.; Jin Kim, Y.; Moon, T.; Seong Hwang, C., *Appl. Phy. Lett.*, **2014**, *104*, 072901.
15. Hyuk Park, M.; Joon Kim, H.; Jin Kim, Y.; Lee, W.; Moon, T.; Seong Hwang, C., *Appl. Phys. Lett.*, **2013**, *102*, 242905.
16. Muller, J.; Boscke, T. S.; Schroder, U.; Mueller, S.; Brauhaus, D.; Bottger, U.; Frey, L.; Mikolajick, T.; *Nano Lett.*, **2012**, *12*, 4318.
17. Marques, A. C.; Almeida, R. M.; *J. Sol-Gel Sci. Technol*. **2006**, *40*, 371
18. Robinson, R. D.; Tang, J.; Steigerwald, M. L.; Brus, L. E.; Herman, I. P.; *Phys. Rev. B* **2005**, *71*.
19. T. Mikolajick, C. D., W. Hartner, I. Kasko, M.J. Kastner, N. Nagel, M. Moert, C. Mazure., *Microelectron. Reliab.* **2001**, *41*, 947
20. Gruverman, A.; Wu, D.; Lu, H.; Wang, Y.; Jang, H. W.; Folkman, C. M.; Zhuravlev, M. Y.; Felker, D.; Rzchowski, M.; Eom, C. B.; Tsymbal, E. Y., *Nano Lett.*, **2009**, *9*, 3539
21. Garcia, V.; Fusil, S.; Bouzehouane, K.; Enouz-Vedrenne, S.; Mathur, N. D.; Barthelemy, A.; Bibes, M., *Nature*, **2009**, *460*, 81.

